WARWICK
THE UNIVERSITY OF WARWICK

Manuscript version: Author's Accepted Manuscript
The version presented in WRAP is the author's accepted manuscript and may differ from the published version or Version of Record.

Persistent WRAP URL:
http://wrap.warwick.ac.uk/170822

How to cite:
Please refer to published version for the most recent bibliographic citation information. If a published version is known of, the repository item page linked to above, will contain details on accessing it.

Copyright and reuse:
The Warwick Research Archive Portal (WRAP) makes this work by researchers of the University of Warwick available open access under the following conditions.

Copyright © and all moral rights to the version of the paper presented here belong to the individual author(s) and/or other copyright owners. To the extent reasonable and practicable the material made available in WRAP has been checked for eligibility before being made available.

Copies of full items can be used for personal research or study, educational, or not-for-profit purposes without prior permission or charge. Provided that the authors, title and full bibliographic details are credited, a hyperlink and/or URL is given for the original metadata page and the content is not changed in any way.

Publisher's statement:
Please refer to the repository item page, publisher's statement section, for further information.

For more information, please contact the WRAP Team at: wrap@warwick.ac.uk.

warwick.ac.uk/lib-publications

This article has been accepted for publication in IEEE Transactions on Transportation Electrification. This is the author's version which has not been fully edited and content may change prior to final publication. Citation information: DOI 10.1109/TTE.2022.3212313

Current Distribution and Anode Potential Modelling in Battery Modules with a Real-World Busbar System

Yaxing Ren, Kailong Liu, *Member, IEEE*, Thomas Grandjean, W. Dhammika Widanage, *Member, IEEE*, James Marco

***Abstract*— The performance of a lithium-ion battery pack is not only related to the behavior of the individual cells within the pack, but also presents a strong interdependency with the temperature distributions, interconnect resistance between cells, and the cell's physical location within the complete battery pack. This paper develops representative busbar circuits with different fidelities to simulate the behavior of cells within a battery module and analyses the influence of cell-to-cell heat transfer and interconnect resistance on the distribution of cell current and anode potential in a battery module. This work investigates multi-physics interactions within the battery module, including cells, interconnect resistances, and temperature distributions, while analyzing the lithium plating problem at the module level. Specifically, the cell model used in this study is a validated thermally coupled single-particle model with electrolyte, and the battery module uses a commercially representative busbar design to include 30-cells in parallel. The effects of parameter changes within the battery pack on individual cells are simulated and analyzed. The study highlights that some cells in the battery module would present a higher risk of lithium plating during fast-charge conditions as they experience a lower anode potential during the charge events.**

***Index Terms*— Current inhomogeneity, busbar design, current distribution, lithium plating, interconnect resistance, cell-to-cell heat transfer**

MATHEMATICAL NOTATION

I	Applied current [A]
V_t	Terminal voltage [V]
ϕ_s^+	Solid electric anode potential [V]
ϕ_s^-	Solid electric cathode potential [V]
$U^{\pm}$	Open circuit potential [V]
$\eta^{\pm}$	Over-potential [V]
$\phi_e^{\pm,s}$	Electrolyte electric potential [V]
$c_{ss}^{\pm}$	Lithium concentration in solid phase at particle surface [mol m^{-3}]
$i_0^{\pm}$	Exchange current density [A m^{-2}]
T	Cell temperature [K]
T_{amb}	Ambient temperature [K]
θ	Volumetric heat capacity of the cell [J m^{-3} K^{-1}]
h	Convective heat transfer coefficient [W m^{-2} K^{-1}]
A	Cooling surface area of the cell [m^2]

I. INTRODUCTION

In recent years, the demand for electrical energy storage has increased significantly with the popularity of intermittent renewable energy and electric vehicles (EVs). Lithium-ion (Li-ion) batteries, currently the most power-dense and commercially mature electrical energy storage technology, have become the dominant choice for power transmission systems [1-3]. In order to meet the mileage requirements of EVs, the power battery is usually composed of hundreds of cells in series and parallel configuration [4, 5]. A variety of factors can cause variations in cell current, temperature, and capacity within parallel-connected battery modules, such as cell manufacturing variability, busbar interconnect resistances and poorly designed thermal management systems [6-8]. In parallel strings, cells with different internal resistances caused by non-ideal busbar design and cell-to-cell temperature variations cause the cells with lower internal resistance to discharge at higher currents and hence generate more heat due to the current inhomogeneity [9, 10]. The variation in cell-to-cell resistance and thermal uniformity limits the total energy capacity of the battery pack, resulting in reduced driving range and divergence of individual cell state of health (SoH) [11-13].

In real EV applications, due to the complexity and cost of installing current sensors in each parallel string, battery management systems (BMS) generally do not monitor the current variation between paralleled cells nor measure the current and temperature of each cell [14]. In this context, the current and temperature sensors are only positioned at strategic locations within the battery pack [15-17]. In addition to this, many recent studies have found that the loss of lithium inventory (LLI) due to lithium plating would greatly reduce the available energy capacity of the battery [18]. But most studies on lithium plating have been undertaken in the context of single

This work is supported by the Faraday Institution Multi-Scale Modelling project [EP/S003053/1 grant number FIRG025]. (*Corresponding author: Kailong Liu*)

Y. Ren was with WMG, University of Warwick, Coventry, CV4 7AL, UK. He is now with the School of Engineering, University of Lincoln, Lincoln, LN6 7TS, UK (e-mail: yren@lincoln.ac.uk).

K. Liu, T. Grandjean, W. D. Widanage and J. Marco are with WMG, University of Warwick, Coventry, CV4 7AL, UK (e-mail: kliu02@qub.ac.uk; t.grandjean@warwick.ac.uk; dhammika.widanalage@warwick.ac.uk; james.marco@warwick.ac.uk).

© 2022 IEEE. Personal use is permitted, but republication/redistribution requires IEEE permission. See https://www.ieee.org/publications/rights/index.html for more information.
Authorized licensed use limited to: University of Warwick. Downloaded on November 02,2022 at 17:37:14 UTC from IEEE Xplore. Restrictions apply.

This article has been accepted for publication in IEEE Transactions on Transportation Electrification. This is the author's version which has not been fully edited and content may change prior to final publication. Citation information: DOI 10.1109/TTE.2022.3212313

cells [19-21] without considering the lithium plating problem in battery modules or packs. In a battery pack, the busbar interconnect resistances on the busbar affect the current distribution in the parallel strings that in turn cause parameter variations across the cells, and eventually manifests more obvious inhomogeneities at the system level [22-24]. Therefore, it is critical to understand the impact of busbar design on current distribution as well as variations in state of charge (SoC), temperature and the potential for lithium plating of cells within parallel strings of battery packs.

To date, only a small number of studies have examined imbalance scenarios based on battery pack models in parallel configurations, and most of these studies have tested or simulated the battery pack consisting of small strings, i.e. only 4-10 cells in parallel [23, 24]. It should be noted that in real EV applications, there are usually more than 30 cells within a module [22]. The limited studies on battery pack degradation have only considered simple one-dimensional Z- or Ladder-configuration connections [25], rather than the real-word cell arrangements used in commercial battery assemblies. Furthermore, in many studies that analyzed the effect of interconnect resistance (R_{IC}) between cells, the value of R_{IC} is usually obtained by measuring the hand soldering resistance in the laboratory [26]. The differences in resistance values between commercial battery busbars and laboratory-based prototypes hand-soldering R_{IC} can greatly affect the relevance and reliability of these research results. At the time of writing, there are no studies in literature which analyze the effects of busbar interconnect resistance on current distribution that include cell-to-cell heat transfer and consider lithium plating within a battery pack with parallel strings. Therefore, the aim of this paper is to predict the current, temperature, SoC, and electrode potentials of each cell within a battery module for mitigating lithium plating conditions by simulating the interactions and heat transfer between the cells and the busbar.

This paper develops models with different fidelity busbar circuit models to simulate the current distribution in a battery module with 30 cells in parallel, and studies the influence of different factors on the current inhomogeneity and anode potential distribution of cells within a representative battery module, making it possible to estimate the lithium plating of individual cells in battery packs. To make the analysis results more relevant to real world usage, the busbar circuit used in this study is from a representative commercial battery module, and the thermally coupled single-particle cell model used to accurately estimate battery lithium plating within the battery pack has been validated with experimental data developed in [27, 28]. Specifically, the main contributions of this work are as follows: 1) Based on the busbar of a commercial battery pack, the busbar circuit models with different fidelity levels are developed and compared with the finite element method model for verification. 2) Compared with previous works where the battery modules are assumed as a simplified ideal parallel or series arrangement, this work investigates multi-physics interactions within the battery module, including cells, interconnect resistances, and temperature distributions. 3) The lithium plating problems are analyzed at the module level, including the influence of different interconnect resistances on the anode potential distribution of cells, and the cells with higher risk of lithium plating in the battery module.

The remainder of this paper is structured as follows: Section 2 details the development of electrochemical cell model, the busbar of the battery module, and thermal model for heat transfer between cells, followed by the description of battery module parameterization process in Section 3. Section 4 presents the result and discussion of cell current, SoC, temperature, anode potential distribution. Section 5 presents the conclusions and further work of this research.

II. Model Development

A. Electrochemical cell model

To account for each cell's dynamic behavior, the pack model used in this study consists of a combination of single cell sub-models. There are two main types of single-cell battery models, namely equivalent circuit models (ECM) and physical based electrochemical models. ECMs are not suitable for our application as they do not contain information about the anode potential required for lithium plating considerations. In order to access unmeasurable physical variables of the cells, the electrochemical model can enable more accurate state estimation [29]. As such, a Thermally-coupled Single Particle Model with electrolyte (TSPMe) is adopted to simulate the performance of individual cells. Terminal voltage, $V_t(t)$, is calculated by [27]:

$$V_t(t) = \phi_s^+(t) - \phi_s^-(t) \tag{1}$$

where $\phi_s^+(t)$ and $\phi_s^-(t)$ represent the cathode (positive) and anode (negative) potentials, respectively. The cathode and anode potentials can be expressed as the sum of the open-circuit voltage (OCV), $U^{\pm}$, overpotential, $\eta^{\pm}$, and electrolyte potential, $\phi_e^{\pm}$, as follows:

$$\phi_s^{\pm}(t) = U^{\pm}\left(c_{ss}^{\pm}(t)\right) + \eta^{\pm}(t) + \phi_e^{\pm}(t) \tag{2}$$

where

$$\phi_e^+(t) = \frac{1}{L_p}\int_{L-L_p}^{L}\left((1-t^+)\frac{2RT}{F}\log\left(\frac{c_e(x,t)}{c_0(x,t)}\right) - \int_0^x \frac{i_e(s,t)}{\sigma_e(c_e(s,t))B(s)}\mathrm{d}s\right)\mathrm{d}x \tag{3}$$

$$\phi_e^-(t) = \frac{1}{L_n}\int_0^{L_n}\left((1-t^+)\frac{2RT}{F}\log\left(\frac{c_e(x,t)}{c_0(x,t)}\right) - \int_0^x \frac{i_e(s,t)}{\sigma_e(c_e(s,t))B(s)}\mathrm{d}s\right)\mathrm{d}x \tag{4}$$

$$\eta^+(t) = \frac{2RT(t)}{F}\frac{1}{L_p}\int_{L-L_p}^{L}\sinh^{-1}\left(\frac{-I(t)}{a_p L_p i_0^+}\right)\mathrm{d}x \tag{5}$$

$$\eta^-(t) = \frac{2RT(t)}{F}\frac{1}{L_n}\int_0^{L_n}\sinh^{-1}\left(\frac{I(t)}{a_n L_n i_0^-}\right)\mathrm{d}x \tag{6}$$

where L_n, L_p, a_n and a_p are the thickness and surface area density of negative and positive electrodes, respectively. L is the total cell thickness. R is the universal gas constant and F is the Faraday constant. $B(x)$ is the geometric factor. σ_e is the ionic conductivity of the electrolyte. c_e is the lithium-ion concentration in the electrolyte. i_e is the current in the electrolyte. $j_0^{\pm}$ is the exchange current density that can be presented as:

$$j_0^{\pm} = m^{\pm}\sqrt{c_e c_{ss}^{\pm}\left(c_{s,\max}^{\pm} - c_{ss}^{\pm}\right)} \tag{7}$$

© 2022 IEEE. Personal use is permitted, but republication/redistribution requires IEEE permission. See https://www.ieee.org/publications/rights/index.html for more information.
Authorized licensed use limited to: University of Warwick. Downloaded on November 02,2022 at 17:37:14 UTC from IEEE Xplore. Restrictions apply.

This article has been accepted for publication in IEEE Transactions on Transportation Electrification. This is the author's version which has not been fully edited and content may change prior to final publication. Citation information: DOI 10.1109/TTE.2022.3212313

where $c_{ss}^{\pm}$ indicates the concentration of lithium-ion in solid surface, $c_{s,\max}^{\pm}$ is the maximum concentration in the electrode, m is the intercalation reaction rate.

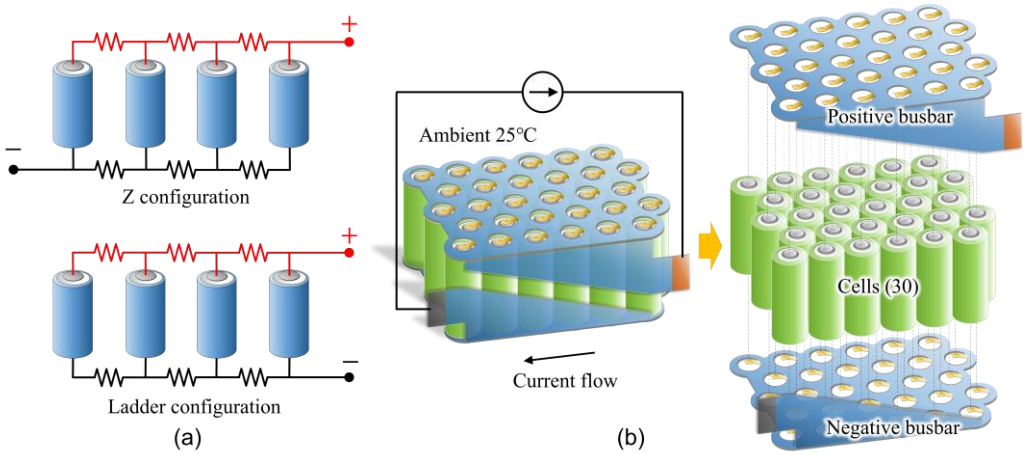

Fig. 1. Modelling of busbar: (a) Traditional Z- or Ladder-configuration; (b) Commercial battery module with cells, connectivity tabs and busbar.

The thermodynamic OCV in the TSPMe model is a function of Li-ion concentration on the surface of the electrodes, which is defined by a mathematical fit to experimental data of voltage and lithium concentration. The OCV is related to the electrode material and the manufacturing process of the cell. It is generally unique to the type, capacity and brand of the target cell and difficult to express in a unified formula. The fitted mathematical equation of OCV used in this study refers to the result in the previous published work [27, 28] and the detailed boundary conditions can also be found from those publications. This information will therefore not be duplicated here.

The thermal behavior of Li-ion cell is given by:

$$\theta \frac{dT(t)}{dt} = I(t) \cdot \left(V_t(t) - U^+(t) + U^-(t)\right) - hA\left(T(t) - T_{\text{amb}}(t)\right) \quad (8)$$

where T is the average temperature of the cell, θ is the volumetric heat capacity of the cell, h is the convective heat transfer coefficient, A is the cooling surface area of the cell, and $T_{\text{amb}}(t)$ is the ambient temperature.

B. Busbar topology of the battery module

Typically in literature, the cell connections are assumed to be one-dimensional connections in a simplified Z-configuration or a Ladder-configuration [22], as shown in Fig. 1 (a). This assumption is not sufficient to accurately simulate the current distribution in a production grade battery module.

As this paper aims to simulate the current distribution in a battery module and its impact on the homogeneity of cell degradation on the basis of a realistic commercial busbar design, this paper adopts the real commercial busbar design from practical applications in order to make the work and its conclusion more realistic. To explore the effects of cell-to-cell variation and thermal gradients on battery pack performance, the commercially representative busbar model from a production EV is used. The commercial busbar is designed considering not only the current input and output direction, but also more complex indices, such as welding, fixing and cooling of cells within the real commercial battery pack. The structure of the battery module is shown in Fig. 1 (b). The battery module is comprised of 30 cells in parallel, and is connected by positive/negative busbars, welded lattices and connectivity tabs. Detailed parameters of the welding process can be found in [30]. For this commercial battery module, 30 cells are divided into 5 columns, while each column consists of 6 single cells arranged in a straight line.

Three different representations of the busbar equivalent circuit (shown in Fig. 2) are proposed in order to investigate the trade-off between model fidelity and the ability to accurately represent individual cell currents and internal states (e.g. SoC). In the first representation, EC1, shown in Fig. 2 (a), all the cells are ideally connected in parallel, with no interconnect resistance (R_{IC}) between the cells. This configuration ignores the influence of R_{IC} in the busbar on the current distribution, which allows the influence of the battery thermal effects on current distribution to be studied independent from R_{IC}.

In the second configuration, EC2, the R_{IC} between columns are considered and shown as black resistors in Fig. 2 (b). However, the R_{IC} within each column is ignored. Therefore, EC2 is equivalent to a one-dimensional structure due to the R_{IC} between columns. Most of the previous work in the literature is based on this assumption. The black resistors represent the lateral equivalent R_{IC} on the battery busbar, and the current flowing through it can be used to represent the current distribution on the busbar. Since commercial busbars are designed to use the least amount of material while meeting the strength and robustness requirements, some metal materials in non-critical positions will be removed to save manufacturing costs. Therefore, when simulating a real commercial busbar, the last column on the right side has only 5 equivalent resistors, while the busbars between other columns have 6 equivalent resistors.

The most complex circuit is EC3, which takes into account the interconnect resistances in both rows and columns based on the geometric connection of each cell in the battery module. It can be found that each individual cell between the row and column has a unique R_{IC} value illustrated as black resistors. In the real commercial busbar, due to the different shapes and

© 2022 IEEE. Personal use is permitted, but republication/redistribution requires IEEE permission. See https://www.ieee.org/publications/rights/index.html for more information.
Authorized licensed use limited to: University of Warwick. Downloaded on November 02,2022 at 17:37:14 UTC from IEEE Xplore. Restrictions apply.

This article has been accepted for publication in IEEE Transactions on Transportation Electrification. This is the author's version which has not been fully edited and content may change prior to final publication. Citation information: DOI 10.1109/TTE.2022.3212313

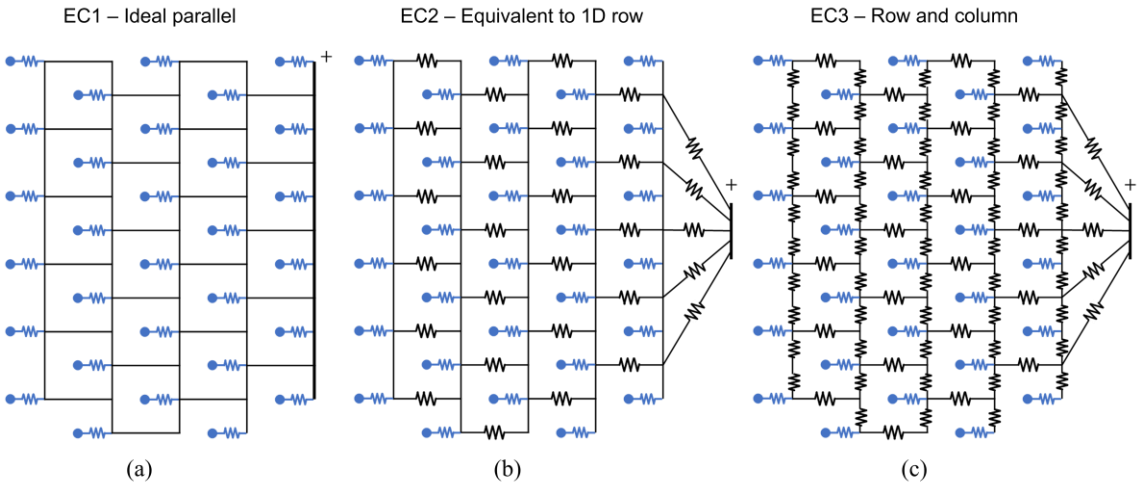

Fig. 2. Equivalent circuit of busbar in a battery module with different complexities.

temperatures on different part of the busbar, the interconnect resistances are different and time-varying. However, these differences are difficult to simulate accurately. Due to the staggered arrangement of the batteries, the interconnection resistances on the busbar are arranged in a hexagonal, like a honeycomb shape. Considering that the material and thickness of the busbars are consistent, and each side of the hexagon is approximately the same length, it is assumed that the resistance values of the six interconnect resistors (represented by black resistors) around each cell in Fig. 2 (c) are all the same. The ohmic resistance value of the metal material is linearly related to the surface temperature. However, due to the small temperature variation range between the cells considered in this paper, the variation range of the resistance at different positions on the busbar affected by temperature can be ignored. Therefore, this paper does not consider the influence of temperature on the change of the R_{IC} value on the busbar.

The welding resistances between each cell and the busbar are shown as blue resistors, whose value highly depends on the quality of the welding process [30] and is assumed to be the same for all cells. Therefore, the welding resistances are independently increased for each cell. Its resistance value will not affect the current distribution in the battery module. Therefore, this paper only discusses the influence of interconnect resistance on the busbar and the influence of welding resistance is not discussed.

C. Heat transfer between cells

To study the effects of cell physical location within the battery module on each cell's individual temperature, the heat transfer between the cells is considered. In commercial battery packs, there is no direct contact between cells. The heat transfer between cells is mainly the convective heat transfer through the side surface of cells and small air gap between cells. The cell terminals are connected to the busbar by welding, so heat can also be transferred via heat conduction through the busbar. In the literature, in addition to surface cooling, there are also terminal cooling configurations [31]. However, the surface of terminal cooling only accounts small amount compared with the side surface of cell, and it will be a challenge for the battery terminals to represent not only the electrical but also the thermal interface [31]. Therefore, the terminal cooling configuration needs further studies before it can become the main cooling configuration. Based on this consideration, this paper only considers the convective heat transfer through the air gaps as the main method of heat transfer between the cells.

Here the battery module contains 30 cells arranged in 5 columns (C) and 6 rows (R), as shown in Fig. 3. For example, C1R1 represents the cell located at the 1st Column and 1st Row of the battery module. Within the module, each cell is surrounded by six adjacent cells, see Cell A in Fig. 3. Thus, a small circular triangular space is formed between each trio of cells for heat transfer. The six sectors of Cell A (C4R4) each exchange heat with two adjacent cells, while Cell B (C1R6) at the edge of module only has two sectors to exchange heat with other cells. The remaining surface of the cell will dissipate heat to the ambient environment.

From literatures [32, 33], the convective heat transfer coefficient is proportional to the thermal conductivity of the air coolant and inversely proportional to the hydraulic diameter of the air cooling channel. For commercial battery modules, the shape and space of air cooling channel are fixed. The thermal conductivity is mainly affected by different air coolants fluid and cooling strategies. According to many publications on battery pack cooling [33, 34], cooling conditions such as cooling air flow rate, flow direction, inlet and outlet temperatures are considered. In order to simplify the battery cooling process, the effects of different cooling conditions and strategies are lumped into the change of the convective heat transfer coefficient in this study. The cooling surface area, A, is calculated as 1/6 of the total surface area of the cylindrical battery, i.e.:

$$A = \pi dl/6 \tag{9}$$

where d and l are the cell diameter and height, respectively. For a 21700 cell, d is 21 mm while l is 70 mm.

In addition to the Li-ion cell self-heating, there is the ohmic heating of the busbar and welds. However, the values of the busbar and weld resistances are much smaller than the internal

© 2022 IEEE. Personal use is permitted, but republication/redistribution requires IEEE permission. See https://www.ieee.org/publications/rights/index.html for more information.
Authorized licensed use limited to: University of Warwick. Downloaded on November 02,2022 at 17:37:14 UTC from IEEE Xplore. Restrictions apply.

This article has been accepted for publication in IEEE Transactions on Transportation Electrification. This is the author's version which has not been fully edited and content may change prior to final publication. Citation information: DOI 10.1109/TTE.2022.3212313

resistance of the cells [23, 24]. Therefore, the heat generated by the busbar and welds is ignored in this study.

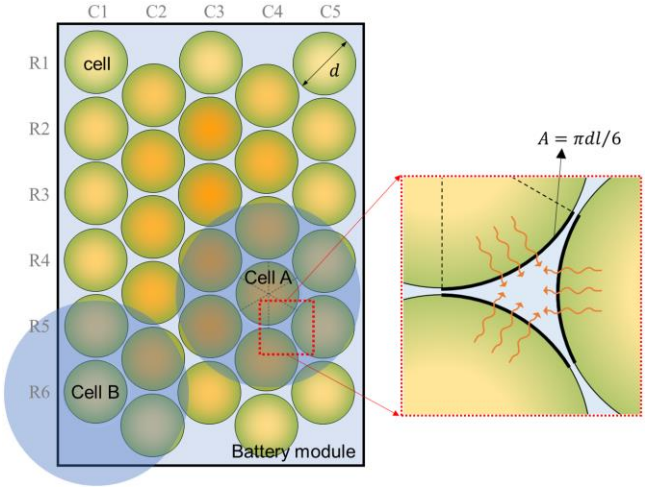

Fig. 3. Heat transfer among cells in densely packed battery module.

III. Battery Module Parameterization

A. TSPMe effective resistance

The Li-ion battery used in this study is based on a 5 Ah cylindrical 21700 cell produced by LG Chem with an operating voltage of 2.5–4.2 V. Here the TSPMe model is calibrated from data obtained by using a three-electrode experiment. In which, the cylindrical cell was disassembled to harvest the electrodes, which are used to fabricate a three-electrode PAT-Cell. The specific experimental procedures and the parameterization process defined in our previous publication [28].

Unlike ECMs, physical based electrochemical models do not use an electrical resistance to represent the internal resistance. For such electrochemical models, the electrolyte diffusion, surface polarization, and back electromotive forces are represented by overpotentials. Therefore, the standard Galvanostatic Intermittent Titration Technique (GITT) test is used to calculate the equivalent internal resistance of the TSPMe cell model.

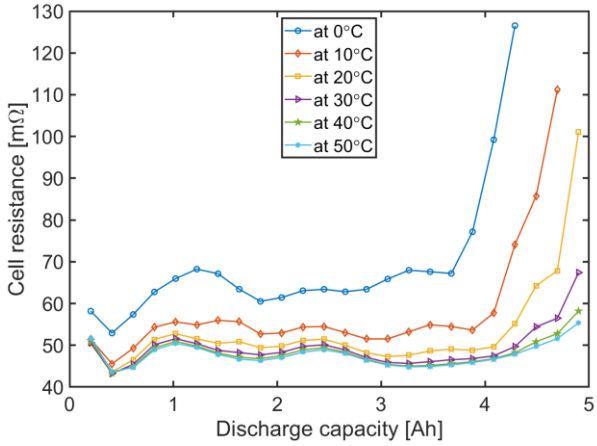

Fig. 4. Effective cell resistance of TSPMe model subjected in a GITT test.

Fig. 4 illustrates the equivalent internal resistance of the TSPMe model at different discharging capacities and temperatures. It can be seen that when the temperature is low, the effective equivalent internal resistance of battery will increase significantly.

B. Busbar FEM simulation

For battery modules, the busbar design affects the current distribution between the cells. For the measurement of R_{IC} on the target commercial busbar, it is difficult to measure the point-to-point interconnect resistance value on the busbar by laboratory methods due to the high integration of the busbar and the complicated paths on the busbar. If dismantling the commercial busbar for measurement, it cannot be guaranteed that the welding resistance is the same as before dismantling. In addition, due to the short distance between cell to cell, the equivalent interconnection resistance on the busbar is only a few to tens of micro-ohms, which also poses a challenge to the measurement accuracy of the laboratory ohmmeter. Based on the above considerations, this paper uses the finite-element simulation method to simulate the busbar of commercial battery module. By importing the design parameters and materials of the commercial busbar, the model and the real object are matched as much as possible. Then the interconnect resistance in the finite-element model (FEM) is used as the reference of actual commercial busbar.

To verify and parameterize the equivalent circuit representing the cell connections, this study refers to the current distribution in the real-world commercial busbar simulated by STAR-CCM+ computational fluid dynamics software as its reference data. Specifically, the busbar model uses FEM based on the busbar geometry and material properties. The purpose here is to simulate the current flow in three-dimensional space within the busbar based on the voltage potential, current density, and temperature distribution within the busbar. An algebraic multigrid-based iterative solver is used in the simulation to ensure the spatial and temporal accuracy and reasonable simulation speed. In order to improve the numerical stability of the simulation, the time step is set to 1 s, and the simulation stop time is set as 30 minutes. During which the battery module model was continuously charged with a constant current of 179 A (about 1.2C). The initial temperature of the cell and the ambient are set to 35 ℃. The temperature, potential, and current at specific locations are extracted from the model of cells and busbars in the battery module. Since the finite element simulation is to simulate the flow of current in three-dimensional space, the current at a certain location is calculated as the root mean square of the current in the x, y, and z directions of the cross-sectional area in the model. Fig. 5 shows an extract from the 3D modelling of current density in the FEM model.

In this study, the FEM model is intended to simulate the current distribution on the busbar rather than the cell behavior within the module. Based upon this consideration, equivalent thermo-sensitive resistors are used in the FEM model instead of Li-ion cells. Therefore, the electrical characteristics of the cells and the resulting current distribution in the busbar can be

© 2022 IEEE. Personal use is permitted, but republication/redistribution requires IEEE permission. See https://www.ieee.org/publications/rights/index.html for more information.
Authorized licensed use limited to: University of Warwick. Downloaded on November 02,2022 at 17:37:14 UTC from IEEE Xplore. Restrictions apply.

This article has been accepted for publication in IEEE Transactions on Transportation Electrification. This is the author's version which has not been fully edited and content may change prior to final publication. Citation information: DOI 10.1109/TTE.2022.3212313

simulated in the FEM model. The thermos-sensitive resistors use the TSPMe effective resistance described in the previous section. The current distribution results from the FE model are used as the reference data for parameterization and comparison of the busbar models in the Simscape simulation environment.

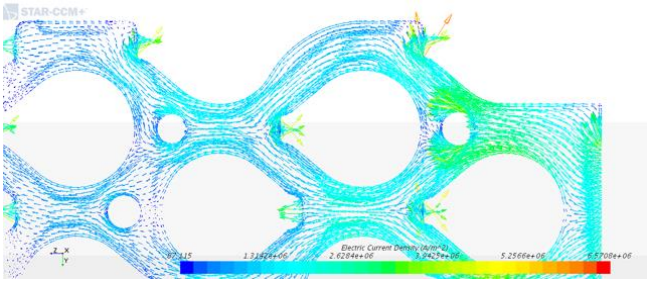

Fig. 5. Simulating the busbar current flow in a FEM model based on the original busbar design.

C. Parameterization of busbar model in Simscape

The busbar model built in Simscape uses the EC3 described in Section 2.2, which is parameterized with the current distribution data of key positions on the busbar in the FEM simulation as a reference. The ohmic value of the interconnect resistance of the simplified busbar model used in Simscape is calculated by dividing the potential difference between adjacent cells in the FEM model by the current at the positions of the interconnect resistances on the busbar. After that, the resistance value is calibrated according to the difference of the current distribution on the interconnect resistances between the FEM model and the Simscape model to achieve the minimum parameter error. After calibration, the comparison of the current values at the positions of the lateral interconnect resistances on the busbar between the FEM model and the Simscape model are shown in Fig. 6. As mentioned earlier, there are only 5 equivalent resistors in the last column on the right side, and 6 equivalent resistors in other columns of busbar, as shown in Fig. 2. Therefore, in the results of FEM model shown Fig. 6, there are only 5 positions on the busbar Column 4.

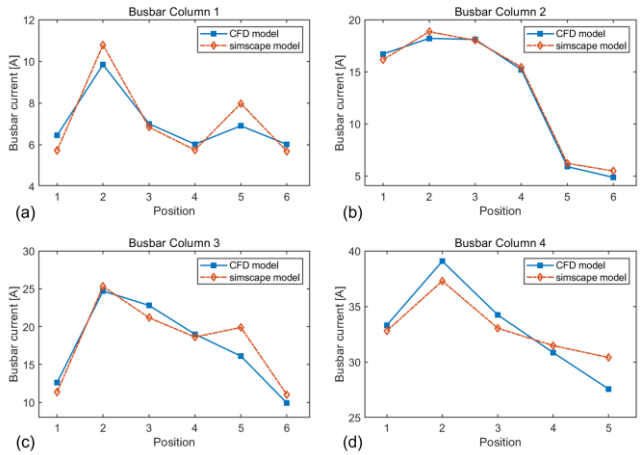

Fig. 6. Comparison between FEM model and Simscape model in busbar current flow simulation.

From the result, the busbar Columns 1, 2, 3 and 4 indicate the position in the middle of the connection bridge between each row and column of battery cells. For example, the cells located at Column 4 are the closest to the current input power source, so the sum of the currents flowing through this column is the total current of the entire battery module. Busbar Column 1 is the position farthest from the current input power supply, so the current passing through its different positions is only the sum of the currents of cells at the most edge position. The average current of the Busbar Column 4 is around four times larger than that of the Busbar Column 1. The current distribution in the Simscape model matches that at specific position from the FE model. This verifies that the busbar circuit of EC3 in Simscape is a good representation of the commercial busbar and can be used to model the current flows of the whole battery module. The Simscape model of the battery module includes a positive busbar, a negative busbar, and 30 TSPMe cell models, whose electrochemical parameters of the cells can be modified accordingly

There are various arrangements of cells in the battery pack, and the arrangement considered in this paper is only one of them, that is, the staggered arrangement of 30 cylindrical cells. Each cell is surrounded by 6 other cells, and the R_{IC} on the busbars are also arranged in a hexagonal, or a honeycomb shape. For other battery module arrangements, such as aligned arrangement battery pack [35], as well as different busbar materials and thicknesses, the ohmic value of the interconnect resistance is likely to be different from that used in this paper.

D. Simscape implementation of battery module

The comparison results between the FEM model and the Simscape model verified that the busbar equivalent circuit in Simscape can achieve similar performance to the FEM model. Therefore, it can be used to build a model of the battery module. The Simscape model of the battery module includes a positive busbar, a negative busbar, and 30 TSPMe cell models, as shown in Fig. 7. The positive and negative busbars have been verified by the FEM model. The 30 cells are thermally and electrically connected in the battery module. The blue lines represent the electrical connections to the positive and negative terminals of the cells. The orange line represents the thermal connection of the cells to their surrounding cells or the ambient temperature.

In the cell model, the equivalent thermo-sensitive resistors are replaced by the TSPMe cell models described in Section 2.1. The electrochemical parameters of the cells can be modified in the cell model. The block "A→B" represents the heat transfer between the cell and the ambient and can set the heat transfer coefficient in the block. The entire battery module is connected to a charger block for setting the current or voltage input and charging mode.

In the simulation of the battery module model, the current flows from the positive terminal of the charger to the positive busbar, and is distributed over the busbar due to the influence of the busbar structure and cell voltage. The current flows into each cell and eventually flows into the negative busbar and back to the negative terminal of the charger. The following section presents the detailed simulation result of the battery module.

© 2022 IEEE. Personal use is permitted, but republication/redistribution requires IEEE permission. See https://www.ieee.org/publications/rights/index.html for more information.
Authorized licensed use limited to: University of Warwick. Downloaded on November 02,2022 at 17:37:14 UTC from IEEE Xplore. Restrictions apply.

This article has been accepted for publication in IEEE Transactions on Transportation Electrification. This is the author's version which has not been fully edited and content may change prior to final publication. Citation information: DOI 10.1109/TTE.2022.3212313

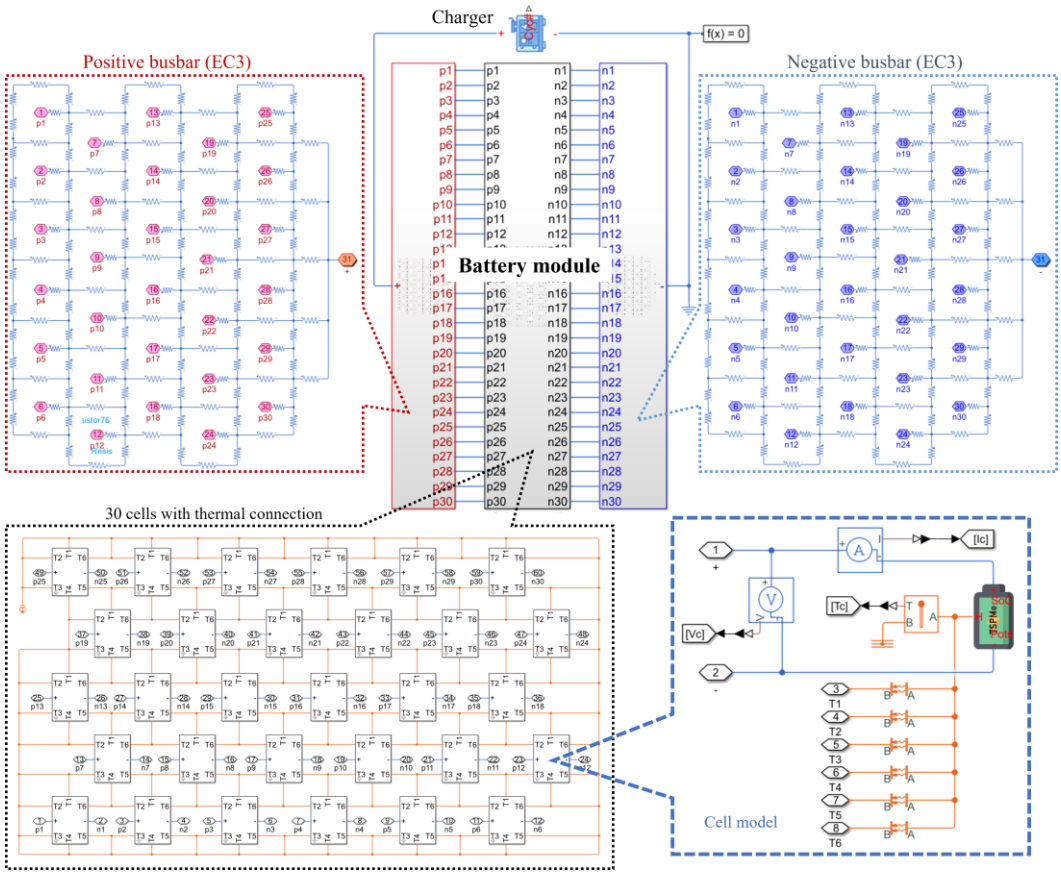

Fig. 7. Implementation of battery module in Simscape

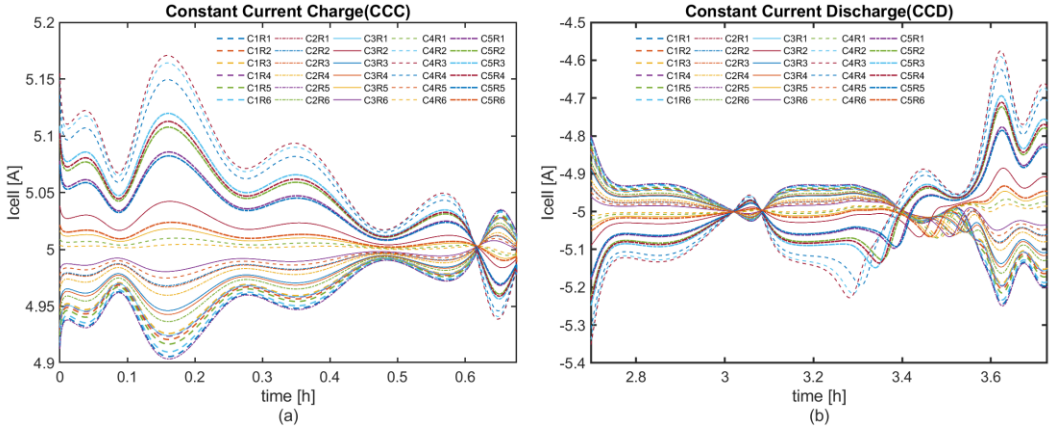

Fig. 8. Current distribution of cells within battery module during CCC and CCD when R_{IC}=0.1 mΩ.

IV. Result and Discussion

An in-depth understanding of the causal relationships between parameter variations and cell current distribution is critical. This section discusses three case studies of the impact of different battery module parameters with 30 TSPMe cells with positive and negative busbars. In this section, the initial capacity, resistance, SoC and thermal boundary conditions of the cells have been defined to be the same for each cell.

A. Impact of different busbar equivalent circuit models

In the simulation based on the LG M50 21700 Li-ion battery, the operating voltage window is 2.5–4.2 V. Fig. 8 shows the current response of all single cells in the battery module for a 1C constant current charge (CCC) and constant current discharge (CCD). The interconnect resistance on the busbar is chosen as a medium value from the range, which is set as 0.1 mΩ. The figure shows the current distribution of 30 cells in the battery module, arranged in 6 rows (R) and 5 columns (C) in a 6×5 battery module.

When the charging current is 1C, the average current of a single cell is approximately 5 A. However, due to the influence of the interconnect resistances (R_{IC} = 0.1 mΩ), there is a significant spread in current distribution between cells. Fig. 8

© 2022 IEEE. Personal use is permitted, but republication/redistribution requires IEEE permission. See https://www.ieee.org/publications/rights/index.html for more information.
Authorized licensed use limited to: University of Warwick. Downloaded on November 02,2022 at 17:37:14 UTC from IEEE Xplore. Restrictions apply.

This article has been accepted for publication in IEEE Transactions on Transportation Electrification. This is the author's version which has not been fully edited and content may change prior to final publication. Citation information: DOI 10.1109/TTE.2022.3212313

shows the largest current during CCC reaches a maximum of 5.17 A and the smallest reaches a minimum of 4.9 A, which is equivalent to a current imbalance of approximately ±3%. This phenomenon is more pronounced in CCD where the current can reach as low as 4.55 A and as high as 5.4 A (±9% current imbalance).

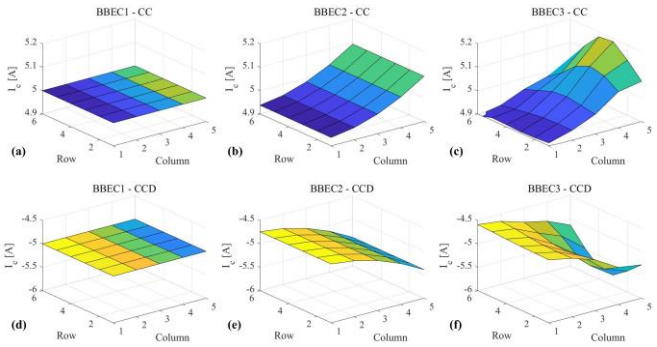

Fig. 9. Current distribution comparison among three different equivalent circuits of busbar under ideal cooling conditions.

To compare the effects of the three different busbar circuits proposed in Section 2.2, the peak current distributions across the busbar circuits during CCC and CCD is shown in Fig. 9. In order to isolate the impact of the busbar on the current distribution, the heat transfer between cells is not considered. The current distribution of charge with EC1, EC2 and EC3 are shown in Fig. 9 (a)-(c), respectively, while that of discharge are shown in Fig. 9 (d)-(f). The results show that in EC1, all cells distribute the total current evenly, so the current distribution surface graph is a flat plane. In EC2, there are some differences in the current distribution across the busbars, where the same current is evenly distributed among the cells in each column, but the R_{IC} between columns causes a gradient in the current variation. In EC3, the effect of the row and column R_{IC} on the current distribution of each cell is modelled. In addition, the results also show that the same cell has the highest current during both charging and discharging. This result highlights the potential for accelerated degradation of cells in that module location.

B. Impact of heat transfer coefficient and interconnection resistance

This section investigates the current distribution in the battery module with different heat transfer coefficients (HTC) and R_{IC} values. Different busbar circuits are used to simulate different scenarios and the impact of busbar fidelities.

In the literature, R_{IC} is often assumed as 1-10% of the rated internal resistance of the cells [22], or fixed to 1-5 mΩ [23-25]. However, these approximations are usually based on laboratory manual welding and are not representative of the welding used in battery module manufacture. From the busbar FEM simulation, the values of the busbar interconnect resistances R_{IC} are significantly smaller than the values commonly used in the literature. Therefore, this paper expands the range of R_{IC} to between 0.01 mΩ and 3 mΩ, which is approximate 0.02%-6% of the rated internal resistance of the LG M50 21700 cells. There are also large variances in the battery module HTC due to the different cooling approaches utilized. A survey of the literature reveals, the typical range of heat transfer coefficient in battery packs are between 5 and 55 $\mathrm{W/m^2K}$ [15, 36-41]. This range is therefore used in this work to investigate the thermal behavior of cells in a battery module.

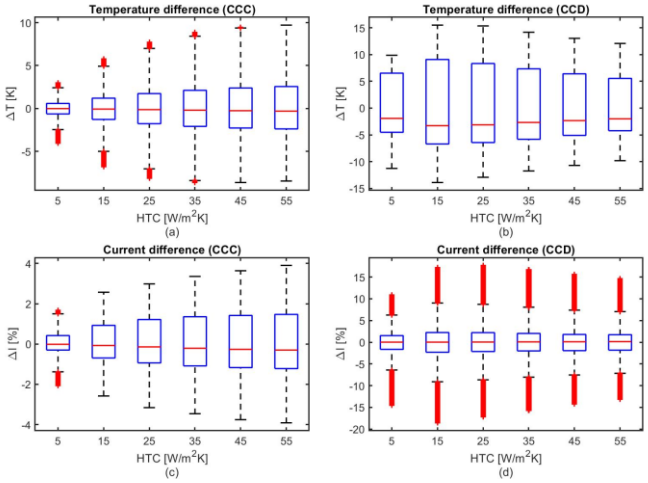

Fig. 10. Variation of cell temperature and current difference in battery module (BBEC1) as heat transfer coefficient increases.

To isolate the effect of different HTC on cell temperature and current distribution, the simulations are performed with EC1 (see Fig. 2) as this busbar ignores the R_{IC} effects. Fig. 10 shows the variation in cell temperature and current distribution for six different HTC values in increments of 5 $\mathrm{W/m^2K}$, covering the range of HTCs commonly used in battery modules in the literature. Since the unite of temperature is in Kelvin, its percentage change is difficult to present the difference in battery temperature at different locations intuitively. The cell temperature variation, ΔT, is calculated as the difference between each individual cell temperature and the average temperature of all 30 cells. A positive value indicates the cell temperature is above the average, while a negative value implies the battery temperature is below the average. Similarly, the battery current range is calculated as the peak value of the positive and negative variations in the cell current, ΔI, divided by the average current to express as a percentage. In the boxplots, the horizontal red line represents the median, the blue box represents the range between the first and third quartiles, and the dashed black line represents the values taken to lie within three standard deviations of the mean. According to the 'three-sigma rule of thumb', the values beyond the three standard deviations are considered as outliers, indicated by red crosses in the boxplot. They represent cell currents or temperatures that exceed the average current and average

© 2022 IEEE. Personal use is permitted, but republication/redistribution requires IEEE permission. See https://www.ieee.org/publications/rights/index.html for more information.
Authorized licensed use limited to: University of Warwick. Downloaded on November 02,2022 at 17:37:14 UTC from IEEE Xplore. Restrictions apply.

This article has been accepted for publication in IEEE Transactions on Transportation Electrification. This is the author's version which has not been fully edited and content may change prior to final publication. Citation information: DOI 10.1109/TTE.2022.3212313

TABLE I

TEMPERATURE AND CURRENT DISTRIBUTION VALUE DURING CCC AND CCD UNDER DIFFERENT HEAT TRANSFER COEFFICIENT.

	h	$5\ \mathrm{W/m^2K}$	$15\ \mathrm{W/m^2K}$	$25\ \mathrm{W/m^2K}$	$35\ \mathrm{W/m^2K}$	$45\ \mathrm{W/m^2K}$	$55\ \mathrm{W/m^2K}$
CCC	$\max(\Delta T)$	2.99 K	5.75 K	7.74 K	8.88 K	9.47 K	9.71 K
	$\min(\Delta T)$	-4.04 K	-6.77 K	-8.15 K	-8.61 K	-8.64 K	-8.46 K
	$\max(I)$ in [A]	5.083 A	5.129 A	5.149 A	5.168 A	5.182 A	5.195 A
	$\min(I)$ in [A]	4.897 A	4.871 A	4.842 A	4.827 A	4.812 A	4.804 A
	$\max(\Delta I)$ in [%]	1.67%	2.57%	2.99%	3.36%	3.64%	3.90%
	$\min(\Delta I)$ in [%]	-2.06%	-2.58%	-3.16%	-3.46%	-3.76%	-3.91%
CCD	$\max(\Delta T)$	9.86 K	15.49 K	15.34 K	14.16 K	13.02 K	12.07 K
	$\min(\Delta T)$	-11.26 K	-13.90 K	-12.92 K	-11.74 K	-10.70 K	-9.82 K
	$\max(I)$ in [A]	-4.455 A	-4.139 A	-4.116 A	-4.161 A	-4.218 A	-4.270 A
	$\min(I)$ in [A]	-5.727 A	-5.928 A	-5.860 A	-5.784 A	-5.711 A	-5.655 A
	$\max(\Delta I)$ in [%]	10.91%	17.22%	17.68%	16.78%	15.64%	14.59%
	$\min(\Delta I)$ in [%]	-14.55%	-18.55%	-17.20%	-15.68%	-14.21%	-13.11%

temperature of the module by more than three standard deviations. Therefore, these cells also need to be observed carefully as they have higher risks of failure in the battery module, including overcurrent, overtemperature, and accelerated degradation. In this paper, the cell inhomogeneity is defined as the percentage difference between the maximum and minimum value. For example, the current inhomogeneity is defined as the highest cell current minus the lowest cell current in the battery module and divided by the average current of the module. Therefore, the higher value of cell inhomogeneity shows the larger difference of cell current or temperature within the battery module.

Since different charging/discharging current will cause different current inhomogeneity, it is clearer to use percentage current difference to represent the proportion of cell current differences. In order to better express the results and quantify the comparison, the detailed data of maximum and minimum value of temperature, current in ampere and current difference in percentage are given in Table I. It can be seen from the results that the spread in cell temperature during charging increases from approximately ±3.5 K to ±9.5 K, while the current distribution spread caused by the temperature inhomogeneity doubles from ±2% to ±4%. During discharge, the battery temperature spread does not increase with increasing values of HTC. The difference between individual cell temperature and the average temperature of all 30 cells reaches a maximum or approximately ±15 K when the HTC is 15 $\mathrm{W/m^2K}$. It reduces with increasing values of HTC to a minimum of approximately ±10 K at 55 $\mathrm{W/m^2K}$. However, the current spread during discharge significantly larger during charge, ranging between ±7% and ±10%.

To investigate the effect of the busbar R_{IC} on current distribution and SoC, the simulations are repeated with EC3 (see Fig. 2) as the busbar circuit. However, in order to isolate the effect of busbar R_{IC}, the heat transfer between cells is ignored. Fig. 11 shows the effect of different interconnect resistance values (0.01 mΩ to 3 mΩ) on the current and SoC spread. The reveals strong positive correlation between R_{IC} and current/SoC spread during both charge and discharge. When the R_{IC} reaches 3 mΩ (approximately 6% of the rated internal resistance of the cell), the highest current is 65% above the average current while the lowest current is 35% below the average current during charging. This means that if the average charge current per cell is 5 A, the maximum current of a single cell can be as high as 8 A, such as cell C5R4 in the module, and the minimum current of cells in the same module is only 3.2 A.

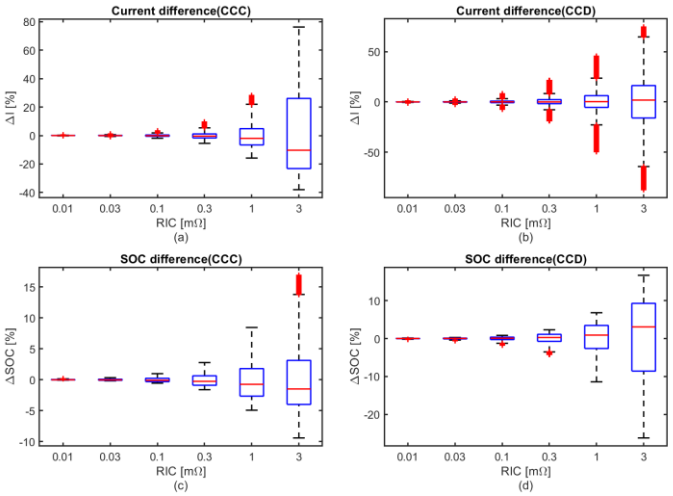

Fig. 11. Variation of cell current and SoC difference in battery module (BBEC3) as interconnect resistance increases.

Since the design of battery busbars and interconnect resistance values vary greatly, this paper gives a wide range of interconnect resistance in order to study its effect on current inhomogeneity. Under normal circumstances, the interconnection resistance of commercial busbars should be much smaller than the case of 3 mΩ. But in extreme cases, such as when the busbar has faults, such as virtual welding, moisture, oxidation, such unexpected value may occur in the interconnection resistance. The current difference represents the transient current imbalance, and the SoC difference represents the accumulation of the current imbalance. Also taking the R_{IC} of 3 mΩ as an example, the highest SoC in the battery pack is 18% higher than the average, and the lowest SoC

© 2022 IEEE. Personal use is permitted, but republication/redistribution requires IEEE permission. See https://www.ieee.org/publications/rights/index.html for more information.
Authorized licensed use limited to: University of Warwick. Downloaded on November 02,2022 at 17:37:14 UTC from IEEE Xplore. Restrictions apply.

This article has been accepted for publication in IEEE Transactions on Transportation Electrification. This is the author's version which has not been fully edited and content may change prior to final publication. Citation information: DOI 10.1109/TTE.2022.3212313

TABLE II
CURRENT AND SOC DISTRIBUTION VALUE DURING CCC AND CCD UNDER DIFFERENT INTERCONNECTION RESISTANCE.

	R_{IC}	0.01 mΩ	0.03 mΩ	0.1 mΩ	0.3 mΩ	1 mΩ	3 mΩ
CCC	max(I) in [A]	5.024 A	5.058 A	5.171 A	5.481 A	6.410 A	CCC
	min(I) in [A]	4.987 A	4.968 A	4.904 A	4.726 A	4.208 A	-8.46 K
	max(ΔI) in [%]	0.49%	1.15%	3.42%	9.62%	28.2%	5.195 A
	min(ΔI) in [%]	-0.26%	-0.64%	-1.92%	-5.47%	-15.8%	4.804 A
	max(ΔSoC)	0.14%	0.33%	0.98%	2.77%	8.44%	3.90%
	min(ΔSoC)	-0.074%	-0.18%	-0.56%	-1.61%	-4.94%	-3.91%
CCD	max(I) in [A]	-4.937 A	-4.852 A	-4.575 A	-3.920 A	-2.711 A	CCD
	min(I) in [A]	-5.049 A	-5.115 A	-5.333 A	-5.881 A	-7.388 A	-9.82 K
	max(ΔI) in [%]	1.26%	2.95%	8.49%	21.6%	45.8%	-4.270 A
	min(ΔI) in [%]	-0.98%	-2.30%	-6.66%	-17.6%	-47.8%	-5.655 A
	max(ΔSoC)	0.13%	0.28%	0.84%	2.31%	6.80%	14.59%
	min(ΔSoC)	-0.25%	-0.59%	-1.68%	-4.14%	-11.4%	-13.11%

which is 11% lower than the average. In other words, the SoC of the cells within the battery pack can vary by up to 29%. This shows that the R_{IC} creates a high degree of imbalance within the battery module during charging. In discharge tests, similar conclusions can be drawn, and the degree of imbalance is higher than in charging. The current disparity can reach up to 1.8 times the average discharge current, and the peak SoC difference can even exceed 25%, as shown in Table II.

For example, when the R_{IC} is 0.1 mΩ, the maximum difference between the battery charging current and the average value is only 3.42%. This means that when the R_{IC} value is smaller than 0.1 mΩ, the current imbalance is mainly caused by the cell temperature differences. When the R_{IC} increases, the effect of the cell temperature difference is smaller than the effect of R_{IC} on the busbar. This result is based on the LG M50 21700 battery. Other cell types may vary, especially if the cell resistance is more sensitive to temperature, the effect of temperature on the current imbalance would be more pronounced.

C. SoC distribution under dynamic current

While the effects of R_{IC} and HTC on current distribution have been verified separately in the last section, the effect of current distribution on SoC non-uniformity was also confirmed. However, there is usually a resting period of at least 30 minutes between regular constant current charging and constant current discharging in the laboratory. This period aims to allow the cells to be stabilized electrochemically and thermally. For the battery module, the resting period will also allow the cells to be rebalanced, that is, the cells are charged and discharged from each other to achieve the same OCV and SoC as there is only inter-cell current flow and no external load applied.

However, in the practical use of battery packs in an electric vehicle, there may be frequent switching between charging and discharging, which does not give a chance for cells to rebalance inside the battery pack. This can cause some cells to charge less than others. This section is mainly to perform a dynamic current test to verify the SoC distribution of the cells inside the battery module in the case of frequent charging and discharging.

Fig. 12 shows the voltage, current, temperature and SoC of the battery module after two complete cycles of constant current charge and constant current discharge with no resting period when the R_{IC} is 1 mΩ and the HTC is 25 $\mathrm{W/m^2K}$. From the

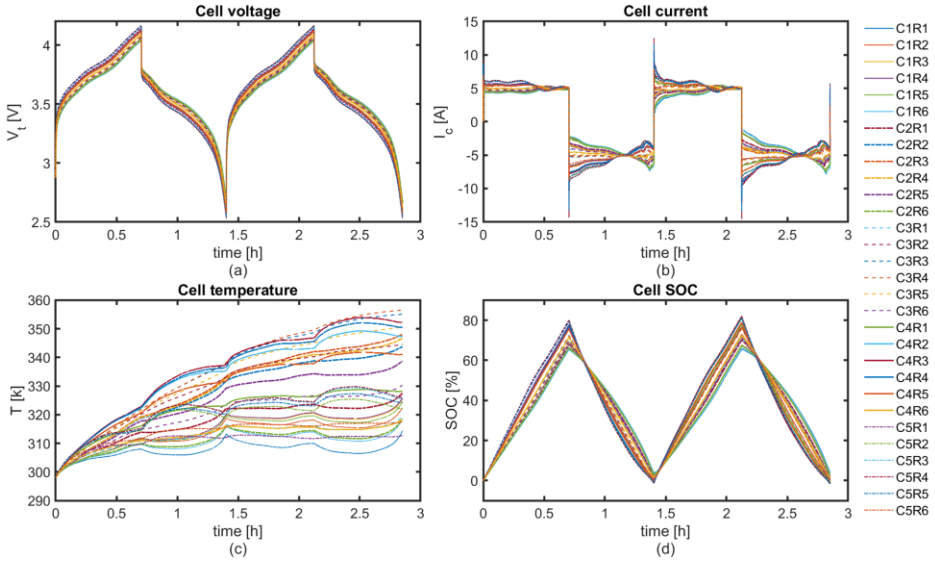

Fig. 12. Cell voltage, current, temperature and SoC distribution under dynamic current loop.

© 2022 IEEE. Personal use is permitted, but republication/redistribution requires IEEE permission. See https://www.ieee.org/publications/rights/index.html for more information.
Authorized licensed use limited to: University of Warwick. Downloaded on November 02,2022 at 17:37:14 UTC from IEEE Xplore. Restrictions apply.

This article has been accepted for publication in IEEE Transactions on Transportation Electrification. This is the author's version which has not been fully edited and content may change prior to final publication. Citation information: DOI 10.1109/TTE.2022.3212313

results in Fig. 12, the current and SoC distributions of the cells are significantly different. For example, the charging current of C1R1 and C1R6 is smaller than that of other cells, resulting in the slowest rise in SoC during charging. Their discharge current is also smaller than other cells. It finally results in that these cells having a lower charge throughput, Q_c, which is calculated by the integration of absolute current flow through the cells in the unite of Ah. In addition to current and SoC, Fig. 12 (c) also shows the changes in cell temperature. The temperature of C3R2, C3R3, C4R3 and C4R4 located in the middle area of the battery module rises the fastest, while the temperature of C1R1 and other cells located at the edge always has the lowest temperature.

The impact of uneven SoC is presented by the charge throughput, which is calculated by integrating the absolute value of current on each cell in the unit of Ah. The charge throughput of all cells after 2 complete charge-discharge cycles are shown in Fig. 13. The cells in each column are represented by the same lines with different colors and marks, and the x-axis represents the position of the cells in each row. It can be seen from the results that the cells with the highest usage rate are located in the 3rd and 4th rows of the column 5, reaching a value of 16 Ah. The cells with the lowest usage rate are located in the 1st and 6th rows of the Column 1, with a value of only 12.3 Ah, which is 23% less than that of the cells with the highest charge throughput value.

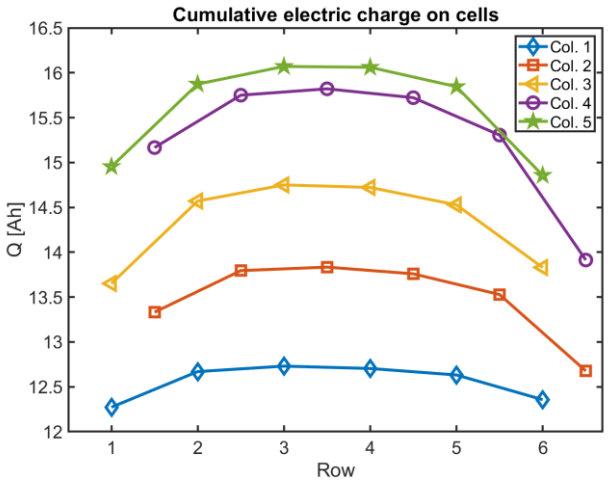

Fig. 13. Charge throughput on each cell after two charge-discharge cycles.

D. Distribution of cell plating depending on anode potential

In addition to the current and temperature distribution effects, this study also considers whether cells will experience lithium plating. When a cell is being charged at high C-rates, there is a risk of the anode potential dropping to a negative value and for lithium plating to occur. Fig. 14 shows the applied current and anode potential distribution of all the cells in the battery module under different R_{IC} during 1C constant current constant voltage (CC-CV). The figure focuses on the section of the charge where the anode potentials are negative. When the R_{IC} is 0.03 mΩ, the cells have similar negative anode potentials as shown in Fig. 14 (a) and (d). As the R_{IC} increases, the current distribution results in different negative anode potentials as shown in Fig. 14 (b) and (e), and when the R_{IC} is 3 mΩ, some cells have a negative anode potential while other are kept positive, as shown in Fig. 14 (c) and (f).

Fig. 14 reveals that for low interconnect resistances ($R_{IC} \leq$ 0.3 mΩ), the lowest anode potential consistently occurs at the transition point from 1C CC to 4.2V CV to prevent the cells from being overcharged and going over the voltage limits defined for the cell. Beyond this voltage there is a higher risk of lithium plating. When the R_{IC} is 0.03 mΩ and 0.3 mΩ, the cells in the battery module are experiencing similar values of anode potential. However, when the R_{IC} rises to 3 mΩ, the individual cell currents and anode potentials are significantly different. In some cells, such as C5R4 in Fig. 14, the lowest anode potential occurs much earlier than the switching point from CC to CV and its anode potential is still decreasing during the CV stage.

Fig. 15 illustrates the lowest cell anode potentials for six R_{IC} values (from 0.01 mΩ to 3 mΩ) depending on the cell location within the module. A different color is used for each column and the y-axis is negative. When the R_{IC} is small, the anode potential distribution of the battery is almost uniform as shown in Fig. 15 (b), (c) and (d). The cells on the edge of the module experience more cooling than the cells within the module. This uneven cooling results in the cells on the edge of the module have slightly higher anode potential.

When the R_{IC} increases: see Fig. 15 (e), (f) and (g), the temperature of the cells close to the power source terminal are higher than the rest of the module. The cells close to the power source have a shorter current path with lower resistance, therefore they draw more current and generate greater heat. Consequently, the anode potential of the cells in Column 4 and 5 are significantly lower than cells in other columns. This indicates that the cells in Column 4 and 5 have a higher risk of lithium plating. The imbalance is most pronounced when the R_{IC} reaches 3 mΩ, see Fig. 15 (g), where the cells in Column 1 and 2 do not have negative anode potentials, and will degrade at a lower rate than the cells in Column 4 and 5.

Fig. 16 (a) and (b) show the cells' current distribution and anode potential distribution, respectively, at the switching point of CC to CV, for six different R_{IC} values (from 0.01 mΩ to 3 mΩ). When the R_{IC} is less than 0.1 mΩ, the cell current 5A, with only ±0.9% to ±2% fluctuation. At the same time, the average anode potential of the cell is 0.043 mV, and the distribution has an inhomogeneity of about ±3 mV to ±4 mV. When the R_{IC} is larger than 0.1 mΩ, the inhomogeneity of the cell current and anode potential distributions increases significantly. The current inhomogeneity increases up to ±41%, and the maximum cell current reaches 7.9 A. At the same time, the anode potential distribution increases to ±35 mV. At $R_{IC} =$ 3 mΩ, some cells have positive anode potentials whilst others are negative, which will result in differential ageing rates as only the later may experience higher levels of lithium plating.

This work has been undertaken on one cell type, namely LG M50 21700 cells, and one commercial busbar design. The conclusions may differ for other cell types and different busbar connection methods, especially for cells that are more sensitive

© 2022 IEEE. Personal use is permitted, but republication/redistribution requires IEEE permission. See https://www.ieee.org/publications/rights/index.html for more information.
Authorized licensed use limited to: University of Warwick. Downloaded on November 02,2022 at 17:37:14 UTC from IEEE Xplore. Restrictions apply.

This article has been accepted for publication in IEEE Transactions on Transportation Electrification. This is the author's version which has not been fully edited and content may change prior to final publication. Citation information: DOI 10.1109/TTE.2022.3212313

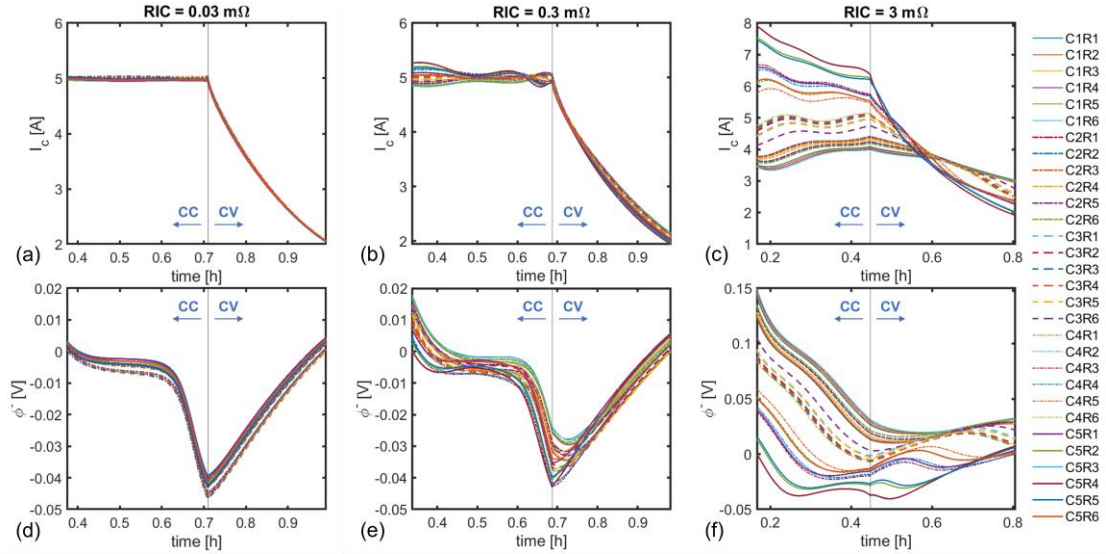

Fig. 14. Anode potential curve under different interconnection resistance.

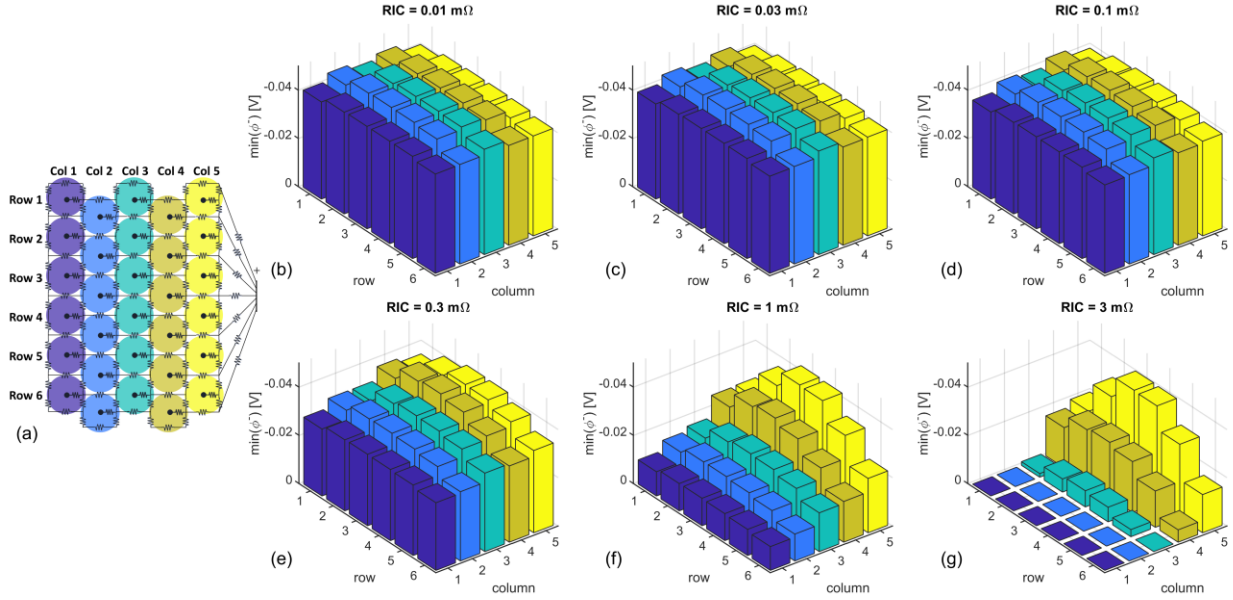

Fig. 15. Cell position of lowest anode potential.

to temperature and variations in SoC. In addition, this paper mainly considers the battery module with cylindrical cells, which is also the most widely used battery today. In addition to this, there are other types such as prismatic battery cells. But each type of cells has its own characteristics in terms of heat dissipation and interconnect resistance. Therefore, the conclusions of this paper cannot be guaranteed to be applicable to all type of cells. But for cell types other than cylindrical cell, they can use similar research methods to analyze the effect of interconnect resistance on the distribution of current, temperature and lithium plating in the battery module.

The cell model used in this paper does not take into account cell degradation or aging. However, it can be seen from previous experiments and literature that the high or low temperature of the battery will cause cell degradation, and more throughputs will accelerate the cell aging. Therefore, although the degradation and aging of cells are not directly modelled and analyzed in this paper, the throughput and temperature of cells at different positions in the battery module are analyzed, which indirectly proves that cells in different positions in the module will have different ageing rate and risk of degradation.

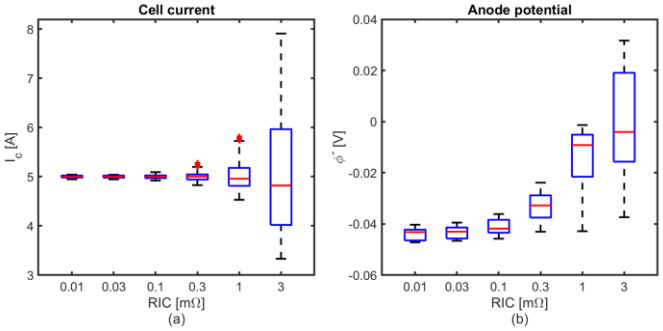

Fig. 16. Distribution of cell current and anode potential

© 2022 IEEE. Personal use is permitted, but republication/redistribution requires IEEE permission. See https://www.ieee.org/publications/rights/index.html for more information.
Authorized licensed use limited to: University of Warwick. Downloaded on November 02,2022 at 17:37:14 UTC from IEEE Xplore. Restrictions apply.

This article has been accepted for publication in IEEE Transactions on Transportation Electrification. This is the author's version which has not been fully edited and content may change prior to final publication. Citation information: DOI 10.1109/TTE.2022.3212313

The research content of this paper has a potential application scenario that is to make it possible for BMS to estimate the state of each cell in the battery module. Currently, the computational power of most BMSs cannot simultaneously estimate the states of dozens or hundreds of cells. The simplified commercial busbar model and the impact of the equivalent interconnect resistance to current and temperature distribution in the battery module studied in this paper can help to reduce the complexity of battery module model. With the development of more powerful microchips, the BMS can realize the function of real-time estimation of the states of each cell in the battery module in the foreseeable future. In future work, the battery busbar model will be validated in an experimental study to further confirm the simulated current inhomogeneities. The impact of heat generated by the busbar and welds will also be considered to add another element of fidelity to the model. In addition, an aging model for the cells will be integrated in future works, and based on this, the model of the battery module will be used to analyze the unevenness of the aging degree of the cells in the battery module after long-term use.

VI. Conclusion

In this paper, according to electrochemical cell models and a representative production busbar circuit, the effects of different factors on the current inhomogeneity and anode potential distribution of cells within a battery pack are analyzed. These factors include cell-to-cell heat transfer coefficient, interconnect resistance on the busbar, and different fidelities of busbar circuit models. It can be seen from the results that when R_{IC} less than 0.2%, the current distribution is mainly caused by temperature distributions from the heat transfer between cells. When R_{IC} becomes over 0.2%, its influence is greater than that of the temperature distribution between cells. The inhomogeneity of current distribution and anode potential exceeds 40%. This study also analyzes the potential for lithium plating issues at the battery module level through some of the most important scenarios and parametric effects, indicating that cells located at certain locations within battery module could present a higher risk of lithium plating. The significance of this work is that it analyses the effect of busbar parameter changes, including R_{IC} and HTC, within the battery pack on individual cells and highlights the important factors for realizing the optimal design of the battery assembly. In light of this, it could benefit the design of observers and optimize control schemes in the BMS in the future to estimate and optimize the current profile, SoC, temperature and lithium plating risk of each cell within the battery module.

References

[1] C. Wang, G. Yin, F. Lin, M. P. Polis, C. Zhang, and J. Jiang, "Balanced control strategies for interconnected heterogeneous battery systems," *IEEE Transactions on Sustainable Energy*, vol. 7, no. 1, pp. 189-199, 2015.

[2] S. Zhang and R. Xiong, "Adaptive energy management of a plug-in hybrid electric vehicle based on driving pattern recognition and dynamic programming," *Applied Energy*, vol. 155, pp. 68-78, 2015.

[3] D. Ren *et al.*, "Model-based thermal runaway prediction of lithium-ion batteries from kinetics analysis of cell components," *Applied energy*, vol. 228, pp. 633-644, 2018.

[4] J. Li and M. S. Mazzola, "Accurate battery pack modeling for automotive applications," *Journal of Power Sources*, vol. 237, pp. 215-228, 2013.

[5] M. Zwicker, M. Moghadam, W. Zhang, and C. Nielsen, "Automotive battery pack manufacturing–a review of battery to tab joining," *Journal of Advanced Joining Processes*, vol. 1, p. 100017, 2020.

[6] S. Santhanagopalan and R. E. White, "Quantifying cell-to-cell variations in lithium ion batteries," *International Journal of Electrochemistry*, vol. 2012, 2012.

[7] S. Paul, C. Diegelmann, H. Kabza, and W. Tillmetz, "Analysis of ageing inhomogeneities in lithium-ion battery systems," *Journal of Power Sources*, vol. 239, pp. 642-650, 2013.

[8] K. Liu, Z. Wei, C. Zhang, Y. Shang, R. Teodorescu, and Q.-L. Han, "Towards long lifetime battery: AI-based manufacturing and management," *IEEE/CAA Journal of Automatica Sinica*, 2022.

[9] X. Wang, Z. Wang, L. Wang, Z. Wang, and H. Guo, "Dependency analysis and degradation process-dependent modeling of lithium-ion battery packs," *Journal of Power Sources*, vol. 414, pp. 318-326, 2019.

[10] X. Gong, R. Xiong, and C. C. Mi, "Study of the characteristics of battery packs in electric vehicles with parallel-connected lithium-ion battery cells," *IEEE Transactions on Industry Applications*, vol. 51, no. 2, pp. 1872-1879, 2014.

[11] X. Feng *et al.*, "Thermal runaway propagation model for designing a safer battery pack with 25 Ah LiNixCoyMnzO2 large format lithium ion battery," *Applied energy*, vol. 154, pp. 74-91, 2015.

[12] F. Sun, R. Xiong, and H. He, "A systematic state-of-charge estimation framework for multi-cell battery pack in electric vehicles using bias correction technique," *Applied Energy*, vol. 162, pp. 1399-1409, 2016.

[13] X. Feng, M. Ouyang, X. Liu, L. Lu, Y. Xia, and X. He, "Thermal runaway mechanism of lithium ion battery for electric vehicles: A review," *Energy Storage Materials*, vol. 10, pp. 246-267, 2018.

[14] C. Pastor-Fernández, T. Bruen, W. Widanage, M. Gama-Valdez, and J. Marco, "A study of cell-to-cell interactions and degradation in parallel strings: implications for the battery management system," *Journal of Power Sources*, vol. 329, pp. 574-585, 2016.

[15] S. Shahid and M. Agelin-Chaab, "Experimental and numerical studies on air cooling and temperature uniformity in a battery pack," *International Journal of Energy Research*, vol. 42, no. 6, pp. 2246-2262, 2018.

[16] S. Shahid and M. Agelin-Chaab, "Development and analysis of a technique to improve air-cooling and temperature uniformity in a battery pack for cylindrical batteries," *Thermal Science and Engineering Progress*, vol. 5, pp. 351-363, 2018.

[17] Y. Jia, M. Uddin, Y. Li, and J. Xu, "Thermal runaway propagation behavior within 18,650 lithium-ion battery packs: A modeling study," *Journal of Energy Storage*, vol. 31, p. 101668, 2020.

[18] C. Zhang *et al.*, "Real-time estimation of negative electrode potential and state of charge of lithium-ion battery based on a half-cell-level equivalent circuit model," *Journal of Energy Storage*, vol. 51, p. 104362, 2022.

[19] S. P. Rangarajan, Y. Barsukov, and P. P. Mukherjee, "Anode potential controlled charging prevents lithium plating," *Journal of Materials Chemistry A*, vol. 8, no. 26, pp. 13077-13085, 2020.

[20] W. Mei, L. Zhang, J. Sun, and Q. Wang, "Experimental and numerical methods to investigate the overcharge caused lithium plating for lithium ion battery," *Energy Storage Materials*, vol. 32, pp. 91-104, 2020.

[21] L. Li *et al.*, "Lithium-ion battery cathode and anode potential observer based on reduced-order electrochemical single particle model," *Journal of Energy Storage*, vol. 44, p. 103324, 2021.

[22] E. Hosseinzadeh *et al.*, "Quantifying cell-to-cell variations of a parallel battery module for different pack configurations," *Applied Energy*, vol. 282, p. 115859, 2021.

[23] T. Bruen and J. Marco, "Modelling and experimental evaluation of parallel connected lithium ion cells for an electric vehicle battery system," *Journal of Power Sources*, vol. 310, pp. 91-101, 2016.

[24] X. Liu, W. Ai, M. N. Marlow, Y. Patel, and B. Wu, "The effect of cell-to-cell variations and thermal gradients on the performance and degradation of lithium-ion battery packs," *Applied Energy*, vol. 248, pp. 489-499, 2019.

[25] R. Luca *et al.*, "Current Imbalance in Parallel Battery Strings Measured Using a Hall-Effect Sensor Array," *Energy Technology*, vol. 9, no. 4, p. 2001014, 2021.

[26] M. J. Brand, E. I. Kolp, P. Berg, T. Bach, P. Schmidt, and A. Jossen, "Electrical resistances of soldered battery cell connections," *Journal of Energy Storage*, vol. 12, pp. 45-54, 2017.

[27] F. B. Planella, M. Sheikh, and W. D. Widanage, "Systematic derivation and validation of a reduced thermal-electrochemical model for lithium-ion

© 2022 IEEE. Personal use is permitted, but republication/redistribution requires IEEE permission. See https://www.ieee.org/publications/rights/index.html for more information.
Authorized licensed use limited to: University of Warwick. Downloaded on November 02,2022 at 17:37:14 UTC from IEEE Xplore. Restrictions apply.

This article has been accepted for publication in IEEE Transactions on Transportation Electrification. This is the author's version which has not been fully edited and content may change prior to final publication. Citation information: DOI 10.1109/TTE.2022.3212313

batteries using asymptotic methods," *Electrochimica Acta*, vol. 388, p. 138524, 2021.

[28] C.-H. Chen, F. B. Planella, K. O'regan, D. Gastol, W. D. Widanage, and E. Kendrick, "Development of experimental techniques for parameterization of multi-scale lithium-ion battery models," *Journal of The Electrochemical Society*, vol. 167, no. 8, p. 080534, 2020.

[29] K. Liu *et al.*, "Electrochemical modeling and parameterization towards control-oriented management of lithium-ion batteries," *Control Engineering Practice*, vol. 124, p. 105176, 2022.

[30] A. Das, A. Barai, I. Masters, and D. Williams, "Comparison of tab-to-busbar ultrasonic joints for electric vehicle Li-ion battery applications," *World Electric Vehicle Journal*, vol. 10, no. 3, p. 55, 2019.

[31] C. Bolsinger and K. P. Birke, "Effect of different cooling configurations on thermal gradients inside cylindrical battery cells," *Journal of Energy Storage*, vol. 21, pp. 222-230, 2019.

[32] H. Park, "A design of air flow configuration for cooling lithium ion battery in hybrid electric vehicles," *Journal of power sources*, vol. 239, pp. 30-36, 2013.

[33] Z. Lu *et al.*, "Parametric study of forced air cooling strategy for lithium-ion battery pack with staggered arrangement," *Applied Thermal Engineering*, vol. 136, pp. 28-40, 2018.

[34] L. H. Saw, Y. Ye, A. A. Tay, W. T. Chong, S. H. Kuan, and M. C. Yew, "Computational fluid dynamic and thermal analysis of Lithium-ion battery pack with air cooling," *Applied energy*, vol. 177, pp. 783-792, 2016.

[35] N. Yang, X. Zhang, G. Li, and D. Hua, "Assessment of the forced air-cooling performance for cylindrical lithium-ion battery packs: A comparative analysis between aligned and staggered cell arrangements," *Applied thermal engineering*, vol. 80, pp. 55-65, 2015.

[36] T. Yang, N. Yang, X. Zhang, and G. Li, "Investigation of the thermal performance of axial-flow air cooling for the lithium-ion battery pack," *International Journal of Thermal Sciences*, vol. 108, pp. 132-144, 2016.

[37] X. Wu, S. Lv, and J. Chen, "Determination of the optimum heat transfer coefficient and temperature rise analysis for a lithium-ion battery under the conditions of Harbin city bus driving cycles," *Energies*, vol. 10, no. 11, p. 1723, 2017.

[38] X. Zhang *et al.*, "Evaluation of convective heat transfer coefficient and specific heat capacity of a lithium-ion battery using infrared camera and lumped capacitance method," *Journal of Power Sources*, vol. 412, pp. 552-558, 2019.

[39] D. Worwood *et al.*, "A new approach to the internal thermal management of cylindrical battery cells for automotive applications," *Journal of Power Sources*, vol. 346, pp. 151-166, 2017.

[40] W. Allafi *et al.*, "A lumped thermal model of lithium-ion battery cells considering radiative heat transfer," *Applied Thermal Engineering*, vol. 143, pp. 472-481, 2018.

[41] M. Akbarzadeh *et al.*, "A comparative study between air cooling and liquid cooling thermal management systems for a high-energy lithium-ion battery module," *Applied Thermal Engineering*, vol. 198, p. 117503, 2021.

© 2022 IEEE. Personal use is permitted, but republication/redistribution requires IEEE permission. See https://www.ieee.org/publications/rights/index.html for more information.
Authorized licensed use limited to: University of Warwick. Downloaded on November 02,2022 at 17:37:14 UTC from IEEE Xplore. Restrictions apply.